Turbulent structures of shock-wave diffraction over 90°convex corner

V. Soni,[1] A. Chaudhuri,[2, a)] N. Brahmi,[1] and A. Hadjadj[1]

[1)] *Normandie University, INSA of Rouen, CNRS, CORIA, 76000 Rouen, France*

[2)] *Department of Civil Engineering and Energy Technology OsloMet — Oslo Metropolitan University, Pilestredet35, PB 4, St. Olavs Plass, 0130, Oslo, Norway*

(Dated: 11 July 2019)

The turbulent structures and long-time flow dynamics of shock diffraction over 90°convex corner associated with incident shock Mach number $M_s = 1.5$, are investigated by large eddy simulation (LES). The average evolution of the core of the primary vortex is in agreement with the previous two dimensional studies. The Type-N wall shock structure is found to be in excellent agreement with the previous experimental data. The turbulent structures are well resolved and resemble to that observed in the experimental findings. Subgrid scale dissipation and subgrid scale activity parameter are quantified to demonstrate the effectiveness of the LES. An analysis based on turbulent non-turbulent interface reveals that locally incompressible regions exhibit the universal teardrop shape of the Joint probability density function of the second and third invariants of the velocity gradient tensor. Stable focus stretching structures (SFS) dominate throughout the evolution in these regions. Stable node/saddle/saddle structures are found to be predominant at the early stage in locally compressed regions and the flow structures evolve to more SFS structures at later stages. On the other hand, the locally expanded regions show mostly unstable nature. From the turbulent kinetic energy, we found that the pressure dilatation remains important at the early stage, while turbulent diffusion becomes important at the later stage. Furthermore, the analysis of resolved vorticity transport equation reveals that the stretching of vorticity due to compressibility and stretching of vorticity due to velocity gradients plays important role compared to diffusion of vorticity due to viscosity as well as the baroclinic term.

Keywords: Shock-wave diffraction, Large Eddy Simulation, Flow topology, Turbulent Kinetic Energy, Vorticity Transport Equation

[a]Electronic mail: arnab.chaudhuri@oslomet.no

I. INTRODUCTION

Study of shock diffraction over various geometries is being active research field for several decades. For example, Griffith & Bleakney[1], addressed the complexity involved in unsteady shock dynamics related to such shock-wave diffraction phenomenon in early 50's. Understanding of shock diffraction is important for internal/external compressible flows involving the propagation of shock waves over solid surfaces e.g., applications like mitigating shock/blast wave with designing effective shock resistant structures. The flow dynamics of these applications involves complex coupled interactions such as shock-shock, shock-vortex, vortex-vortex, and shock-turbulence interactions. Along with experimental approaches, with the advent of numerical techniques, numerical studies gained popularity for addressing intricate issues associated with such complex flow dynamics. Two-dimensional (2D) inviscid simulations[2–5] are capable of resolving the general features associated to shock-wave diffraction. Most of the studies in literature relied upon the inviscid predictions, to establish the basic wave characteristics. Among these, Baum et al.[4] presented a 2D numerical study of complex geometry canisters using adaptive finite element based shock capturing scheme. Subsequently, several qualitative studies addressed the shock wave interaction with the compressible vortex associated to shock diffraction[6–10] problems. Viscous effects are important to resolve the long-time evolution of shock-vortex dynamics and shock-boundary layer/ shock-shear layer interactions. High-order scheme based numerical solvers equipped with robust shock capturing capabilities are essential to resolve the shock dynamics as well as the wide range of length/time scales of the turbulence. In this regard, several studies utilised high-order Weighed Essentially Non Oscillatory WENO based schemes[11–17] or Discontinuous spectral element method (DSEM) with artificial viscosity[18–20] to address complex flow features associated with shock diffraction, shock propagation, shock focusing, shock obstacle interaction etc. Unsteady three-dimensional (3D) studies of shock diffraction are not abundant in literature. Reeves & Skews[21] studied the evolution of spiral vortex for 3D edges ('V', 'inverted-V', 'parabolic' and 'inverted parabolic' types). A general and preliminary three-dimensional study of the merging of vortices resulting from shock diffraction and vortex shedding off a discontinuous edge is presented by Cooppan & Skews[22]. Also, Skews & Bentley[23] addressed a 3D analysis of the merging of two diffracting shocks.

In a recent study[19], the authors revisited the shock diffraction over 90°convex corner and addressed some intricate features of resolving the viscous and turbulent flow features. The main issues related to the 2D numerical predictions of this flow dynamics are to address the experimentally observed i) secondary viscous vortex associated with the wall shock interaction with the boundary layer and ii) the shear layer behavior (see e.g., Takayama & Inoue[24], Sun & Takayama[6] for detail of this canonical benchmark case). These are addressed with a high-order numerical scheme based predictions by Chaudhuri & Jacobs[19]. It can be realised from the relatively recent experiments (e.g., see Skews et al.[25] and Law et al.[26]) that, the shear layer structures associated with the long-time evolution exhibit fine turbulent flow structures.

It is evident that 3D simulations and analysis are required to shed light into the turbulent structures and shear layer instabilities observed in these experiments. To the best of our knowledge, analysis of 3D flow features associated with shock diffraction over sharp corners has never been reported before. The objective of this work is to perform large eddy simulation (LES) to explore the 3D turbulent flow structures and analyse the long-time behavior of the shock diffraction over 90°convex corner with incident shock Mach number $M_s = 1.5$. The paper is organized as follows. In section III, a brief description of the methodology is described. The numerical setup is presented in section 1, followed by the results and discussions in section IV. Finally conclusions are drawn in section V.

II. PROBLEM SET-UP

Moving shock wave of shock Mach number $M_s = 1.5$ is allowed to pass through a 90°convex corner having a rectangular cross section of 35mm×25mm. The step height h, is taken as 140mm and the step length is set to 25mm. The problem set-up of the simulation is shown in figure 1. The mesh resolution of the computational domain of 200mm×175mm×35mm (length-height-width) is summarised in table I. The initial location of the moving shock is positioned at 75% of the step length. Rankine-Hugoniot relations are used to set the initial conditions for left (shocked stated) and right (stagnant state) states associated with the chosen M_s. Air is considered as working fluid and the initial stagnant state is assigned with temperature $T = 288$K and pressure $p = 101325$ Pa. The spanwise (z-direction) direction is considered as homogeneous direction and periodic boundary conditions are applied at these boundaries. The left and right boundaries (x-direction) are kept as the initial conditions and simulations are executed avoiding any reflections from these boundaries. We apply symmetry condition at the top boundary and adiabatic no-slip boundary conditions are set for the remaining solid walls. To assign realistic velocity fluctuations, homogeneous isotropic turbulent velocity fluctuations are superimposed with the initial velocity field in the shocked gas region.

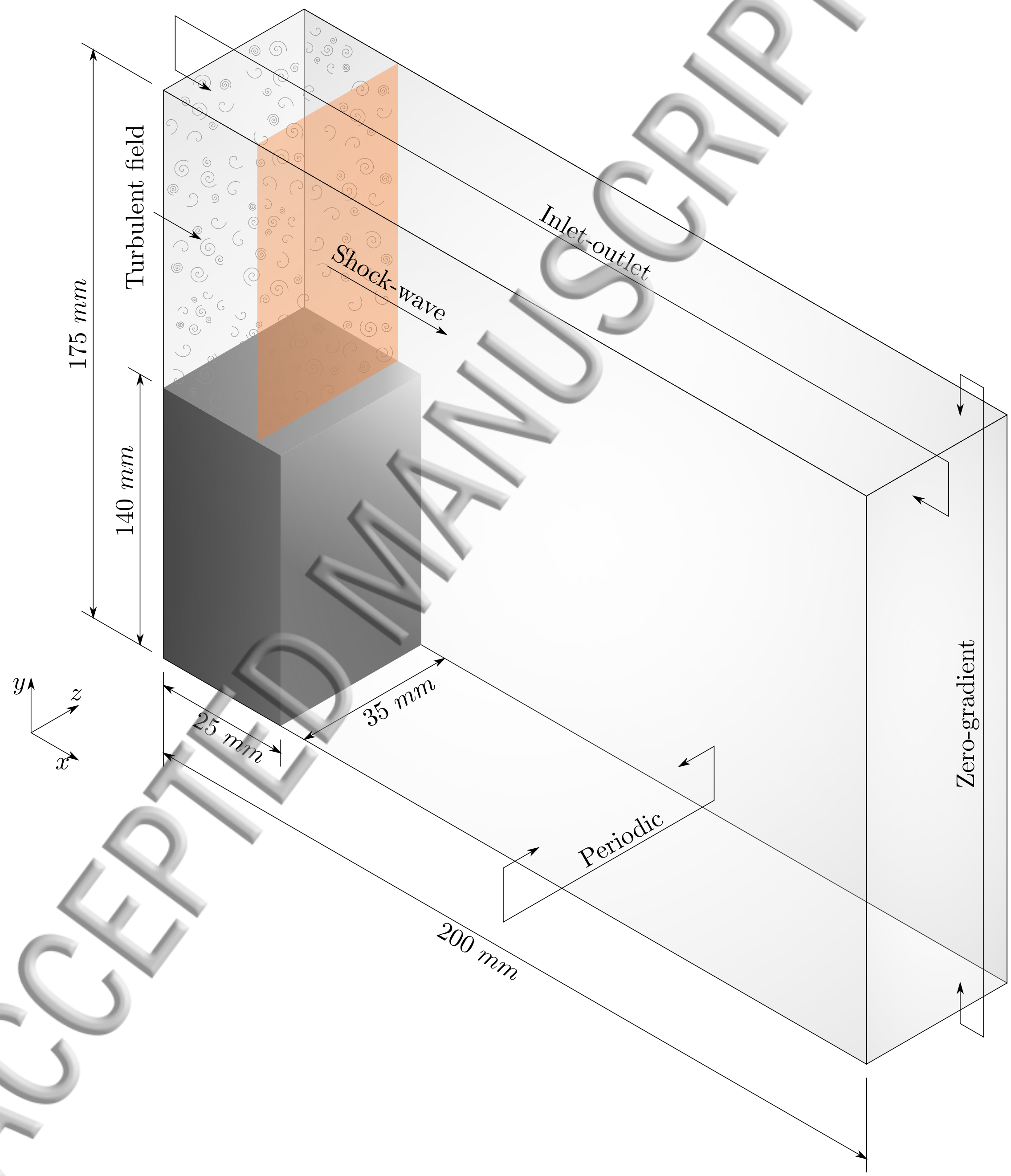

FIG. 1: Schematic diagram of the problem set-up.

TABLE I: Simulation parameters.

Total no. of Meshes	Δx	Δy	Δz	final time t
3.3 billion	52.6μm	51.4μm	136.7μm	757.75μs

III. METHODOLOGY

We solve the filtered compressible Navier Stokes system of equations to simulate the diffraction of the moving shock, over a convex corner. The definition of any filtered quantity with a filtered function G_Δ and filter width $\Delta = (\Delta_x \times \Delta_y \times \Delta_z)^{1/3}$ is given by $\bar{\phi}(\vec{x},t) = \int_{R^3} \phi(\vec{\eta},t)G_\Delta(\vec{x}-\vec{\eta})d\vec{\eta}$. Favre averaged quantities $\tilde{\phi} = \overline{\rho\phi}/\bar{\rho}$ are used to reduce subgrid scale (SGS) terms. The in-house parallel compressible flow solver equipped with immersed boundary method is used for this purpose. Fifth-order WENO scheme is used for inviscid fluxes and sixth-order central difference scheme is used for viscous fluxes. A third-order explicit Runge-Kutta method is used to advance in time. The SGS stress and SGS heat flux terms are closed by the wall adapting local eddy viscosity (WALE) model. For brevity, the filtered governing equations, LES model, and the immersed boundary methodology are not presented here, the details are available in our previous works[12,27–29]. The immersed boundary method (we use trilinear interpolation see Soni et al.[29]) in 3D simulations and LES model constants are essentially similar to those mentioned in these references. The flow solver is validated with relevant standard benchmark problems and reported in our previous works. It is to be noted that, only resolved quantities are used for the analysis and discussions below. The resolved fluctuating component of any parameter is obtained by subtracting the spatially averaged (along the homogeneous z-direction) resolved quantity from the corresponding instantaneous resolved parameter as defined as: $\phi'' = \widetilde{\phi} - \langle\widetilde{\phi}(x,y,t)\rangle$, where $\langle\widetilde{\phi}(x,y,t)\rangle = \dfrac{1}{L_z}\displaystyle\int_{L_z} \widetilde{\phi}\, dz$.

To reduce the complexity of the notation, the resolved quantities are expressed without overbar $\overline{(\cdot)}$ or tilde $\widetilde{(\cdot)}$ notation in most of the discussions below. This means $\widetilde{\phi_i} \equiv \phi_i$. To have better clarity, only the notations for the turbulent kinetic energy budget equation are presented with actual notations.

IV. RESULTS AND DISCUSSIONS

A. General description and validation

The shock diffraction over 90°diffraction corner is associated with complex coupled interactions like shock-vortex, shock-boundary layer, vortex-vortex and shock-shock interactions. Studies in literature show that, 2D Euler predictions sufficiently agree with the early stage of the general shock dynamics, but suffers from inability to resolve secondary vortex formation due to boundary layer interactions with the wall shock. Nevertheless, high-resolution 2D Navier-Stokes simulations with consideration of viscous/turbulent effects can predict these behavior well[19,29]. This canonical benchmark problem of diffraction is being studied in literature by several authors, but no 3D numerical studies are available to account for the long-time behavior of turbulent flow structures. Experimental observations show existence of these 3D structures (see Skews et al.[25] and Law et al.[26]). The LES performed in this study demonstrates these structures. The early and later stages shock dynamics and the complex interactions are presented in figure 2 and compared favorably with the experimental results. Especially, the present LES resolved the intricate turbulent structures illustrated by the numerical schlieren pictures. A detailed analysis of turbulent flow features is presented in the remaining sections below.

The convective Mach number $\left(M_c = \dfrac{U_1 - U_c}{a_1} = \dfrac{U_c - U_2}{a_2}\right)$ at various locations at $t =$ 757.75 μs are found to be 0.53 at A*, 0.43 at B*, 0.29 at C* and 0.16 at D* (see figure 3 for the locations of the measurements of M_c). Here $U_c = \dfrac{a_1 U_2 + a_2 U_1}{a_1 + a_2}$. Also, U_1 and U_2 are the free stream velocities across the shear layer and a_1 and a_2 are the respective speeds of the sound. The shear layer behavior shows prominent compressibility effects near the diffraction corner (A*) and progressively shifts towards near incompressible regime around D*.

We analyze the sufficiency of the domain length in the homogeneous direction via two-point autocorrelation function given by:

$$R_{\phi\phi}(r_z) = \sum_{n=1}^{N_z} \phi''_n \phi''_{n+n_r}, \qquad n_r = 0, \ldots, N_z - 1 \; ; \; r_z = n_r \Delta z \tag{1}$$

Figure 4 shows the autocorrelation distributions for velocity fluctuations at different probe locations A to D (see figure 3). The curves degenerate to near zero values within the half of the domain length in the homogeneous direction. The domain size is thus sufficient

TABLE II: Nomenclature: general description and validation.

Abbreviations	Full-form
I	Incident shock wave
DS	Diffraction shock wave
EW	Expansion shock wave
CS	Contact surface
SL	Shear layer
KHI	Kelvin-Helmholtz instabilities
V	Vortex core
VV	Viscous vortex
VS	Vortex shock
LS	Lambda shock

enough so that, the periodic boundary condition does not inhibit the turbulence in spanwise z-direction.

The accuracy of the LES is further checked by computing the normalized energy spectra of the fluctuating velocity components. These are shown in figure 5 together with the $-5/3$ law. These spectra show similar behavior of the peak values and exhibit drop off of about two decades. The large turbulent scales of the flow features are well resolved by the current LES and SGS dissipation takes into account the dissipation effects of very fine scales. The effectiveness of the WALE model and SGS activity are illustrated in subsection IV B.

Figure 6 shows the locus of the vortex centroid and the comparison with the previous 2D numerical results of Sun & Takayama[6]. The wall shock for the present case is of Type-N as classified in Matsuo et al.[3]. Note that, an excellent agreement of the shape of the wall shock with the experimental results of Skews[30] is predicted by the present simulation. The circulation, $\Gamma = \int_{\boldsymbol{s}} \omega \, d\boldsymbol{s}$ is computed over the 3D interaction region and is illustrated in figure 7. The circulation rate is non-dimensionalised with the property of the air at stagnant state, $RT = 287 \times 288 \ m^2/s^2$. The non-dimensional circulation is found to be attaining a saturation value of ≈ 1.2. However, Sun & Takayama[7] reported a circulation rate of 1.36 based on their 2D study.

The turbulent and non-turbulent regions for different turbulent flows are separated by a distinct boundary having several interesting characteristics like entrainment, abrupt changes in turbulence properties and intermittency. The shape of this interface is influenced by all scales of turbulence in general. Vorticity norm or passive scalar concentration or concentration field can be used to define this turbulent-nonturbulent interface (TNTI)[31–36]. To do this, we use the mean magnitude of the vorticity at each x-y plane. The 30% of it is then set as the threshold value to define a TNTI parameter as: $\mathrm{TNTI}_z = 0.3\overline{|\omega|}_z,\ \ z = 1, \ldots, N_z$. A location is considered inside the turbulent region if the magnitude of its local vorticity is higher than the TNTI_z in that x-y plane. Figure 3 depicts the inner turbulent region covered by the TNTI surface at $t = 757.75\ \mu s$. The choice of the threshold value is intuitive and these contours effectively identify the vortex dominated turbulent regions for further analysis. The irrotational engulfed pockets are also visible in this figure. Rotational dominated regions of the flow field can be illustrated from the normalised Q-criteria[37,38], $\Lambda = \dfrac{W_{ij}W_{ij} - S_{ij}S_{ij}}{W_{ij}W_{ij} + S_{ij}S_{ij}}$. Where $S_{ij} = 1/2(\partial u_i/\partial x_j + \partial u_j/\partial x_i)$ is the strain-rate tensor, and $W_{ij} = 1/2(\partial u_i/\partial x_j - \partial u_j/\partial x_i)$ is the rotation-rate tensor. The positive iso-surfaces of Λ shown in figure 8, illustrates the vortex tubes and 3D turbulent flow features.

B. SGS model assessment

In this section, we present the relative contribution of SGS dissipation and assess the effectiveness of the WALE model. The ratio of μ_{sgs}/μ is the measure of effectiveness of the LES model. Figure 9 shows the time evolution of the spatially averaged contours of μ_{sgs}/μ (averaged in homogenous z-direction) in the interaction zone. The ratio, $\mu_{sgs}/\mu \leq 5$ indicates that the grid resolution and the contribution of SGS viscosity is in the acceptable range for well resolved LES. The SGS modeled dissipation ε_{sgs} can be defined as[28] the summation of contribution of fluctuating flow-field to SGS dissipation and the contribution of mean flow-field to SGS dissipation as:

$$\varepsilon_{sgs} = \varepsilon''_{sgs} + \varepsilon_{\langle sgs \rangle} \tag{2}$$

The contribution of fluctuating flow-field to SGS dissipation approximated as:

$$\varepsilon''_{sgs} \approx -2\langle \mu_{sgs} S''^{*}_{ij} S''_{ij} \rangle \tag{3}$$

where, $S''_{ij} = \frac{1}{2}\left(\frac{\partial u''_i}{\partial x_j} + \frac{\partial u''_j}{\partial x_i}\right)$ and $S''^{*}_{ij} = S''_{ij} - \frac{1}{3}S''_{kk}\delta_{ij}$.

The contribution of mean flow-field to SGS dissipation can be expressed as:

$$\varepsilon_{\langle sgs\rangle} \approx -2\langle\mu_{sgs}\rangle\langle S^*_{ij}\rangle\langle S_{ij}\rangle \tag{4}$$

where, $\langle S_{ij}\rangle = \frac{1}{2}\left(\frac{\partial\langle u_i\rangle}{\partial x_j} + \frac{\partial\langle u_j\rangle}{\partial x_i}\right)$ and $\langle S^*_{ij}\rangle = \langle S_{ij}\rangle - \frac{1}{3}\langle S_{kk}\rangle\delta_{ij}$.
The details of these approximations can be found in Ben-Nasr et al.[28] and Davidson[39].

Figure 10 shows the different SGS dissipation parameters (averaged in homogeneous z-direction) in the interaction zone at different time instants. It can be seen from this figure that, ε''_{sgs} contributes more towards ε_{sgs} compared to $\varepsilon_{\langle sgs\rangle}$. The contours of $\frac{\varepsilon_{sgs}}{\varepsilon}$ show a similar range of values of μ_{sgs}/μ as mentioned before. This corroborates the fact that the mesh resolution in the shear layer region is sufficient for this LES study. The modeling effectivity of a LES can also be quantified with the SGS activity parameter, as defined by

$$\zeta = \frac{\varepsilon_{sgs}}{\varepsilon_{sgs} + \varepsilon} \tag{5}$$

where, the resolved molecular dissipation $\varepsilon = \left\langle \tau''_{ij}\frac{\partial u''_i}{\partial x_j}\right\rangle$. Evidently, $0 \leq \zeta < 1$, and the lower the value of ζ the more resolved is the LES. It could be noted that the vortex core region is very well resolved by the current LES. These are in accordance with the 3D flow visualisation of resolved flow structures illustrated with the iso-surfaces of $\Lambda = 0.5$ in figure 8.

C. Analysis on the local flow topology

The flow topology analysis based on the turbulent/non-turbulent interface (TNTI) which separates the inner core of the turbulent region from the neighborhood of the irrotational regions is much revealing and enriching to characterize the zonal turbulent flow structures. Literature shows that the locally compressed regions in a turbulent flow field are dominated by stable topological structures. While, the locally expanded regions are mainly unstable in nature and more dissipative. In this section, we present the flow topology associated with the dynamics of the shear layer at the 90° diffraction corner. The invariants of the velocity (resolved) gradient tensor (P, Q and R) are given by:

$$\boldsymbol{P} = -S_{ii} \tag{6}$$
$$\boldsymbol{Q} = \frac{1}{2}(\boldsymbol{P}^2 - S_{ij}S_{ji} - W_{ij}W_{ji}) \tag{7}$$
$$\boldsymbol{R} = \frac{1}{3}(-\boldsymbol{P}^3 + 3\boldsymbol{P}\boldsymbol{Q} - S_{ij}S_{jk}S_{ki} - 3W_{ij}W_{jk}S_{ki}) \tag{8}$$

where S_{ij} and W_{ij} are strain-rate tensor and rotation-rate tensor as defined before.

It is well known that the $P - Q - R$ space is divided into several regions[40–45]. The discriminant surface $\mathscr{L}_1$, of the characteristic equation of the eigenvalues of the velocity gradient tensor, separates the region of real and complex eigenvalues. This can be further split into $\mathscr{L}_{1a}$ and $\mathscr{L}_{1b}$. All eigenvalues are real and equal at a location where these surfaces form a cusp. On the other hand, purely imaginary eigenvalues lie on the surface $\mathscr{L}_2$ (see equations 13).

The second invariant of W_{ij} is given by,

$$\boldsymbol{Q_w} = -\frac{1}{2}W_{ij}W_{ji} \tag{9}$$

The surfaces dividing the $P - Q - R$ space are,

$$\mathscr{L}_1 = 27\boldsymbol{R}^2 + (4\boldsymbol{P}^3 - 18\boldsymbol{P}\boldsymbol{Q})\boldsymbol{R} + (4\boldsymbol{Q}^3 - \boldsymbol{P}^2\boldsymbol{Q}^2) = 0 \tag{10}$$
$$\mathscr{L}_{1a} = \frac{1}{3}\boldsymbol{P}\left(\boldsymbol{Q} - \frac{2}{9}\boldsymbol{P}^2\right) - \frac{2}{27}\left(-3\boldsymbol{Q} + \boldsymbol{P}^2\right)^{3/2} - \boldsymbol{R} = 0 \tag{11}$$
$$\mathscr{L}_{1b} = \frac{1}{3}\boldsymbol{P}\left(\boldsymbol{Q} - \frac{2}{9}\boldsymbol{P}^2\right) + \frac{2}{27}\left(-3\boldsymbol{Q} + \boldsymbol{P}^2\right)^{3/2} - \boldsymbol{R} = 0 \tag{12}$$
$$\mathscr{L}_2 = \boldsymbol{P}\boldsymbol{Q} - \boldsymbol{R} = 0 \tag{13}$$

We summarize the nomenclature of the invariants and various 3D critical points in table III.

The evolution of the PDF of the first invariant of the velocity gradient tensor is shown in figure 11. A self-similar behavior with highly peaked distribution has been found. A large positive skewness of the distributions clearly depicts the similar behavior observed in the compressible isotropic turbulence and compressible mixing layer turbulence of literature[42]. The JPDFs of the $Q - R$ are shown for constant P planes. Three representative values of P are chosen to distinguish the features of locally incompressible, compressed and expanded regions in the flow-field. Here, Q and R are normalized with Q_w and $Q_w^{3/2}$ in these figures. Table IV summarizes all the quantities of the local flow topology for different dilatation

TABLE III: Nomenclature: local flow topology.

Abbreviations	Full-form
$\boldsymbol{P}$	First invariant of the velocity gradient tensor
$\boldsymbol{Q}$	Second invariant of the velocity gradient tensor
$\boldsymbol{R}$	Third invariant of the velocity gradient tensor
$\boldsymbol{Q_w}$	Second invariant of the rotation-rate tensor
UFC	Unstable focus compressing
UN/S/S	Unstable node/saddle/saddle
SN/S/S	Stable node/saddle/saddle
SFS	Stable focus stretching
SFC	Stable focus compressing
UFS	Unstable focus stretching

levels at different time instants. Evidently, the sample size is large at a later time instant. Note that the % of TNTI is large for $P = 0$ compared to locally compressed and expansion regions. This corroborates with highly peaked distribution of PDF of P mentioned before. For incompressible turbulent flows ($P = 0$), the JPDF of second and third invariants (Q and R) of the velocity gradient tensor exhibits a typical tear drop shape (see Figure 12). This signifies the universal small-scale structures of turbulence. The similar universal tear drop shape is also being found for compressible flows when the JPDF of second and third invariants of the anisotropic part of the deformation rate tensor are analyzed. This is similar to the characteristics of incompressible turbulence, compressible isotropic turbulence, compressible turbulent boundary layer and compressible mixing layer turbulence. Clearly the SFS structure dominates throughout the evolution with an increasing trend of SFS structure with time (95.5% at 757.75μs).

Figure 13 depicts JPDFs of $Q - R$ for locally compressed regions. The shape of these distributions evolves to nearly tear drop shape. However, it can be seen from table IV, that a dramatic distribution of the topologies is existent. Initially, we observe dominant non-focal stable structures (48.1% of SN/S/S). Most of the structures remain stable for compressed regions. Nevertheless, the unstable structures are also found to be present. The initial SN/S/S structures shifts towards SFS structures. Although, there exists some more unstable structures compared to locally incompressible regions, the stable structures are predominant in locally compressed regions.

Figure 14, shows the JPDFs for locally expanded regions. The distributions are found to be skewed towards the surface $\mathscr{L}_2$ and most of the flow structures show unstable nature. The present analysis reveals the absence of UFS for locally compressed region and the absence of SFC for locally expanded regions. UN/S/S structures eventually becomes predominant in these regions. The unstable structures indeed become significant for locally expanded regions. It can be realized that the local streamlines in stable topologies are convergent towards critical points and for unstable topologies the local streamlines are divergent from the critical points.

TABLE IV: Quantification of the flow topology enclosed by TNTI as a percentage of their sample size.

Dilatation	Time (μs)	Quantity (% of TNTI)	Sample ($\times 10^6$)	UFC	UN/S/S	SN/S/S	SFS	SFC	UFS
	251.75	10.4	2.7	5.0	6.3	7.8	80.7	-	-
$\boldsymbol{P} = 0 \pm 0.05$	449.75	9.8	8.5	3.2	3.7	2.2	90.9	-	-
	757.75	14	33.4	1.1	1.6	1.6	95.6	-	-
	251.75	0.2	0.05	11.6	7.1	48.1	21.8	9.8	-
$\boldsymbol{P} = 3 \pm 0.25$	449.75	0.3	0.2	12.3	10.4	24.8	44.5	6.9	-
	757.75	0.2	0.4	10.8	10.2	17.2	55.9	5.8	-
	251.75	0.1	0.03	18.7	25.1	4.7	24.8	-	23.9
$\boldsymbol{P} = -3 \pm 0.25$	449.75	0.2	0.2	17.7	30.8	2.6	30.7	-	16.9
	757.75	0.1	0.3	16.9	34.1	3.3	31.1	-	12.9

D. Analysis of the turbulent kinetic energy

The Favre averaged transport equation of turbulent kinetic energy (TKE) is given by,

$$\underbrace{\frac{\partial \bar{\rho} k}{\partial t} + \frac{\partial \bar{\rho} \tilde{u}_j k}{\partial x_j}}_{\mathcal{A}} = \underbrace{-\langle \rho u_i'' u_j'' \rangle \frac{\partial \tilde{u}_i}{\partial x_j}}_{\mathcal{P}} \underbrace{-\left\langle \tau_{ji} \frac{\partial u_i''}{\partial x_j} \right\rangle}_{\mathcal{D}} \underbrace{+\frac{\partial}{\partial x_j} \left(\langle \tau_{ji} u_i'' \rangle - \left\langle \rho u_j'' \frac{1}{2} u_i'' u_i'' \right\rangle - \langle p' u_j'' \rangle \right)}_{\mathcal{D}_f}$$
$$\underbrace{-\langle u_i'' \rangle \frac{\partial \bar{p}}{\partial x_i}}_{\mathcal{P}_w} \underbrace{+\left\langle p' \frac{\partial u_i''}{\partial x_i} \right\rangle}_{\mathcal{P}_d} \tag{14}$$

where, $\mathcal{P}$ is the production term, $\mathcal{D}$ is the dissipation term, $\mathcal{D}_f$ is the diffusion term, $\mathcal{P}_w$ is the pressure-work term, $\mathcal{P}_d$ is the pressure-dilatation term, and $\mathcal{A}$ is the advection term. Note that, we kept the overbar $\overline{(\cdot)}$ or tilde $\widetilde{(\cdot)}$ notation here for better clarity.

The spatially averaged contours of these resolved terms are shown in figures 15, 16 and 17. The behavior of the TKE budget terms of the shear layer region is found to be typically similar to the compressible mixing layers (see Chaudhuri et al.[38]). These contours also show the out of equilibrium behavior of the turbulent flow linked with the transient flow evolution. The pressure dilatation and pressure work terms are associated with the regions of shear layer near the diffraction corners (having high convective Mach numbers) as well as regions where the interactions of the shocklets and the core of the vortex are significant. It can be seen that sporadic patches of negative production of turbulent kinetic energy are also predicted. These are associated with the regions with shear layer/vortex interactions with local compressions/expansions[27,46,47]. We analyse the time evolution of the magnitude of these terms and their cross-correlations within the spatiallay averaged two dimensional turbulent region bounded by the TNTI. These are shown in figures 18 and 19. At the early stage, the pressure dilatation term remains important, and the diffusion term plays major role in the later stage. Diffusion, production, and pressure dilatation terms are found to be nearly one order of magnitude higher than pressure work and dissipation. Note that, the pressure dilatation is more correlated to dissipation term at the beginning and evolves to a state with more correlated with pressure work at the later stage. The overall anti-correlation is evident between production and dissipation terms. Pressure dilatation and pressure work remain linked with dissipation. Noticeably, the diffusion term is found to be anti-correlated with the pressure dilatation term throughout the evolution. It can be realized that the diffusion terms interact with the outer regions of the shear layer through the edges of the shear layer. The advection term is found to be predominantly linked with pressure work apart from the other terms.

E. Analysis of the vorticity transport equation

We further analyse the budget terms of the mean vorticity transport equation (equation 15) to shed light into the large scale structures and the mechanism of the complex flow evolution associated with the shock diffraction phenomena. The contribution of SGS terms can be assumed to be negligible for the mutual interactions among the relatively large vortical structures. The nomenclature of the different terms of the transport equation are summerised in table V.

$$\frac{\partial \boldsymbol{\omega}}{\partial t} + (\boldsymbol{u} \cdot \nabla)\boldsymbol{\omega} = \underbrace{(\boldsymbol{\omega} \cdot \nabla)\boldsymbol{u}}_{\mathcal{V}_g} - \underbrace{\boldsymbol{\omega}(\nabla \cdot \boldsymbol{u})}_{\mathcal{V}_c} + \underbrace{\frac{1}{\rho^2}\nabla\rho \times \nabla p}_{\mathcal{B}} + \underbrace{\nabla \times \left(\frac{\nabla \cdot \tau}{\rho}\right)}_{\mathcal{D}_v} \tag{15}$$

The evolution of the contours of these terms are shown in figure 20. VSC, VSG, DFV and baroclinic terms interplay during the evolution process. From the VSC contour, it is clear that there are locally stretched structures in the core region of the vortex due to compressibility effect arising from local regions of compression/expansion. The evolution of enstrophy is illustrated in figure 21. This corroborates to saturation of the magnitude of the enstrophy. The time evolution of the magnitude of these terms and their cross-correlations within the 3D turbulent region bounded by the TNTI are analysed further. Note that the magnitude of the VSG term and VSC term are nearly one order of magnitude higher compared to the baroclinic term and DFV term (see figure 22). Indeed, VSG plays major role transferring the turbulent energy from large scales to small scales in flows at high Reynolds number as found in Cottet et al.[48]. Positive correlation of VSG and VSC is observed (see figure 23). However, enstrophy is found to be predominently correlated with VSG compared to VSC. Furthermore viscous effects via DFV term is anticorrelated with enstrophy. DFV is also found to be anticorrelated with VSG, which is in accordance with the contours shown in figure 20.

V. CONCLUSION

In this work, we presented a 3D analysis of turbulent flow features originating from a shock wave diffraction over 90°convex corner that has never been attempted before. The intricate features of the viscous effects, shock boundary layer interactions, shock shear layer

TABLE V: Nomenclature: vorticity transport equation (VTE).

Abbreviations	Full-form
VSC ($\mathcal{V}_c$)	Stretching of vorticity due to compressibility
VSG ($\mathcal{V}_g$)	Stretching/tilting of vorticity due to velocity gradients
$\mathcal{B}$	Baroclinic torque
DFV ($\mathcal{D}_v$)	Diffusion of vorticity due to viscosity
$\mathcal{E}$	Enstrophy

interactions are well addressed by this analysis. LES with WALE model together with high-order numerical schemes (fifth order WENO for inviscid, sixth order central differencing for viscous fluxes, third order explicit Runge-Kutta scheme for the time advancement) are chosen to resolve the complex flow scales. The in-house parallel solver used 3.3 billion cells to resolve the flow structures. The general dynamics of vortex core and shape of the Type-N wall shock have been compared with the literature data[30] favorably. The chosen domain size in spanwise direction is demonstrated to be sufficient enough through the behavior of autocorrelation functions. The effectiveness of the LES model and the mesh resolution characteristics are quantified by SGS viscosity and SGS dissipation. The 3D flow visualisation with rotation dominated regions by normalised Q criteria shows the quality of the current well resolved LES. The 3D instantaneous field resembles to the turbulent scale structures observed in the experimental findings[25]. We performed a flow topology analysis based on TNTI. The JPDFs of the second and third invariants (Q and R) of the velocity gradient tensor are used for constant (first invariant) P planes for this purpose. Locally incompressible regions exhibit the teardrop shape of the PDF of Q and R indicating the universal nature of the resolved smaller scales of the turbulence. We found that, SFS structures are dominating throughout the flow transients in these regions. SN/S/S structures remain predominant at the early stage in locally compressed regions, and at the later stage, the flow structures evolve to more SFS structures. Although unstable strucures are found to be present relatively more compared to locally incompressible regions. On the other hand, we found mostly unstable structures at the locally expanded regions. The present analysis also reveals the absence of UFS for locally compressed region and the absence of SFC for locally expanded regions. Neglecting the SGS contributions, the turbulent kinetic energy budget terms are analysed with only resolved parameters. This reveals that the pressure dilatation is important at the early stage, while turbulent diffusion becomes important at later stages and the diffusion term exhibits anti-correlation with the pressure dilatation term throughout the flow evolution. Furthermore, the relative contribution of the constituent terms of the resolved mean vorticity transport equation is analysed. The VSC and VSG plays important role compared to DFV, and baroclinic term and enstrophy is predominantly correlated with VSG compared to VSC.

The 2D viscous simulations of shock-wave diffraction over 90° sharp corner with high resolution numerical scheme can predict the basic shock diffraction wave pattern, main vortex, secondary viscous vortex associated with the wall shock interaction with the boundary layer, shear layer, lambda shocks observed in the experiments specially at the early stage of the evolution. However, 2D simulations are limited to resolve the inherent 3D nature of the turbulent flow features and together with the small-scale dissipation. The present 3D LES captures the 3D turbulent scales, embedded shocks/shocklets within the main vortex and the shear layer behavior and boundary layer interactions in the viscous vortex region. The spatio-temporal growth of the shear layer is strongly influenced by the lambda shock as well as by the counter-clock-wise rotating viscous vortex near the diffraction corner. Apparently, the lambda-shock-shear-layer interaction at the upper side of the shear layer is more intense than that of the interaction of the contact surface at the bottom side of the shear layer. Note that, the foot of the lambda shock more effectively perturbs the shear layer and increases its growth. This aspect is clearly resolved in the present LES. The shape and large-scale structures of the turbulent envelop at the wall viscous vortex region is also satisfactorily predicted by the LES. A further investigation regarding the mechanism and possible influence (upstream and downstream) of the contact surface at the underside of the shear layer could be addressed in future work.

Future works will be undertaken to address the performance of different LES models resolving this complex flow dynamics. Detailed analysis of the local entrainment across the TNTI can be explored for the compressible turbulent shear layer. The present LES is performed with 3 billion mesh points and can be considered as well resolved, however, further ensemble averaging could be attempted[27] with phase-incohorence in the initial isotropic turbulence to make stable flow statistics and detailed analysis towards the local mechanisms of the complex evolution. From the large-scale tests of Skews et al.[25], it appears that several lambda shocks could play an important role towards large-scale KH instabilities at later stage of the shear layer development. Also, the onset of the decay of the turbulence in the viscous vortex zone due to viscous dissipation is evident from the experimental findings. These long-time flow features could be investigated further to enhance the understanding of the complex flow dynamics.

ACKNOWLEDGMENTS

This study was supported by the BIOENGINE project, which is funded by the European Regional Development Fund (ERDF) and the Regional Council of Normandie, under contract HN-0002484. This work was performed using computing resources from Centre Rgional Informatique et d'Applications Numriques de Normandie (CRIANN), Rouen, France.

REFERENCES

[1] W. C. Griffith and W. Bleakney, "Shock waves in gases," Am. J. Phys. **22**, 597–612 (1954), https://doi.org/10.1119/1.1933855.

[2] I. I. Glass, J. Kaca, D. L. Zhang, H. M. Glaz, J. B. Bell, J. A. Trangenstein, and J. P. Collins, "Diffraction of planar shock waves over halfdiamond and semicircular cylinders: An experimental and numerical comparison," AIP Conference Proceedings **208**, 246–251 (1990), https://aip.scitation.org/doi/pdf/10.1063/1.39456.

[3] K. Matsuo, T. Aoki, and H. Kashimura, "Diffraction of a shock wave around a convex corner," AIP Conference Proceedings **208**, 252–257 (1990), https://aip.scitation.org/doi/pdf/10.1063/1.39458.

[4] J. D. Baum, E. Loth, and R. Löhner, "Numerical simulation of shock interaction with complex geometry canisters," AIP Conference Proceedings **208**, 909–914 (1990).

[5] S. Sivier, E. Loth, J. Baum, and R. Löhner, "Vorticity produced by shock wave diffraction," Shock Waves **2**, 31–41 (1992).

[6] M. Sun and K. Takayama, "A note on numerical simulation of vortical structures in shock diffraction," Shock Waves **13**, 25–32 (2003).

[7] M. Sun and K. Takayama, "Vorticity production in shock diffraction," J. Fluid Mech. **478**, 237–256 (2003).

[8]P. Halder, S. De, K. Sinhamahapatra, and N. Singh, "Numerical simulation of shock–vortex interaction in schardins problem," Shock Waves **23**, 495–504 (2013).

[9]R. Ripley, F.-S. Lien, and M. Yovanovich, "Numerical simulation of shock diffraction on unstructured meshes," Comput. Fluids **35**, 1420–1431 (2006).

[10]G. Abate and W. Shyy, "Dynamic structure of confined shocks undergoing sudden expansion," Prog. Aerosp. Sci. **38**, 23–42 (2002).

[11]A. Chaudhuri, A. Hadjadj, O. Sadot, and G. Ben-Dor, "Numerical study of shock-wave mitigation through matrices of solid obstacles," Shock Waves **23**, 91–101 (2013).

[12]A. Chaudhuri, A. Hadjadj, O. Sadot, and E. Glazer, "Computational study of shock-wave interaction with solid obstacles using immersed boundary methods," Int. J. Numer. Meth. Eng. **89**, 975–990 (2012).

[13]A. Chaudhuri, A. Hadjadj, O. Sadot, and G. Ben-Dor, "Study of shock-wave mitigation through solid obstacles," in *28th International Symposium on Shock Waves*, edited by K. Kontis (Springer Berlin Heidelberg, Berlin, Heidelberg, 2012) pp. 493–498.

[14]A. Chaudhuri, A. Hadjadj, and A. Chinnayya, "On the use of immersed boundary methods for shock/obstacle interactions," J. Comput. Phys. **230**, 1731–1748 (2011).

[15]E. Glazer, O. Sadot, A. Hadjadj, and A. Chaudhuri, "Velocity scaling of a shock wave reflected off a circular cylinder," Phys. Rev. E **83**, 066317 (2011).

[16]M. Shadloo, A. Hadjadj, and A. Chaudhuri, "On the onset of postshock flow instabilities over concave surfaces," Phys. Fluids (1994-present) **26**, 076101 (2014).

[17]V. Soni, A. Hadjadj, A. Chaudhuri, and G. Ben-Dor, "Shock-wave reflections over double-concave cylindrical reflectors," J. Fluid Mech. **813**, 7084 (2017).

[18]A. Chaudhuri, G. Jacobs, W. Don, H. Abbassi, and F. Mashayek, "Explicit discontinuous spectral element method with entropy generation based artificial viscosity for shocked viscous flows," J. Comput. Phys. **332**, 99 – 117 (2017).

[19]A. Chaudhuri and G. B. Jacobs, "Dynamics of shock wave diffraction over sharp splitter geometry using entropy-based artificial viscosity method," Shock Waves **29**, 101–115 (2019).

[20]A. Chaudhuri, "Shock propagation and diffraction through cavity," in *Proceedings of The 59th Conference on Simulation and Modelling (SIMS 59), 26-28 September 2018, Oslo Metropolitan University, Norway*, 153 (Linkping University Electronic Press, Linkpings universitet, 2018) pp. 111–117.

[21]J. O. Reeves and B. Skews, "Unsteady three-dimensional compressible vortex flows generated during shock wave diffraction," Shock Waves **22**, 161–172 (2012).

[22]S. Cooppan and B. Skews, "Three-dimensional shock wave diffraction off a discontinuous edge," Shock Waves **27**, 131–142 (2017).

[23]B. Skews and J. Bentley, "Merging of two independent diffracting shock waves," Shock Waves , 1–5 (2016).

[24]K. Takayama and O. Inoue, "Shock wave diffraction over a 90 degree sharp cornerposters presented at 18th issw," Shock waves **1**, 301–312 (1991).

[25]B. Skews, C. Law, A. Muritala, and S. Bode, "Shear layer behavior resulting from shock wave diffraction," Exp. Fluids **52**, 417–424 (2012).

[26]C. Law, A. Muritala, and B. Skews, "Unsteady flow with separation behind a shock wave diffracting over curved walls," Shock Waves **24**, 283–294 (2014).

[27]A. Chaudhuri and A. Hadjadj, "Numerical investigations of transient nozzle flow separation," Aerosp. Sci. Technol. **53**, 10 – 21 (2016).

[28]O. Ben-Nasr, A. Hadjadj, A. Chaudhuri, and M. S. Shadloo, "Assessment of subgrid-scale modeling for large-eddy simulation of a spatially-evolving compressible turbulent boundary layer," Comput. Fluids **151**, 144–158 (2017).

[29]V. Soni, A. Hadjadj, and O. Roussel, "On the use of adaptive multiresolution method with time-varying tolerance for compressible fluid flows," Shock Waves **29**, 37–50 (2019).

[30]B. W. Skews, "The shape of a diffracting shock wave," J. Fluid Mech. **29**, 297304 (1967).

[31]C. B. da Silva and J. C. F. Pereira, "Invariants of the velocity-gradient, rate-of-strain, and rate-of-rotation tensors across the turbulent/nonturbulent interface in jets," Phys. Fluids **20**, 055101 (2008), https://doi.org/10.1063/1.2912513.

[32]M. Gampert, J. Boschung, F. Hennig, M. Gauding, and N. Peters, "The vorticity versus the scalar criterion for the detection of the turbulent/non-turbulent interface," J. Fluid Mech. **750**, 578596 (2014).

[33]T. Watanabe, Y. Sakai, K. Nagata, Y. Ito, and T. Hayase, "Turbulent mixing of passive scalar near turbulent and non-turbulent interface in mixing layers," Phys. Fluids **27**, 085109 (2015), https://aip.scitation.org/doi/pdf/10.1063/1.4928199.

[34]R. Jahanbakhshi, N. S. Vaghefi, and C. K. Madnia, "Baroclinic vorticity generation near the turbulent/ non-turbulent interface in a compressible shear layer," Phys. Fluids **27**, 105105 (2015), https://doi.org/10.1063/1.4933250.

[35]G. Borrell and J. Jimnez, "Properties of the turbulent/non-turbulent interface in boundary layers," J. Fluid Mech. **801**, 554596 (2016).

[36]R. Jahanbakhshi and C. K. Madnia, "Entrainment in a compressible turbulent shear layer," J. Fluid Mech. **797**, 564603 (2016).

[37]P. Davidson, *Turbulence: an introduction for scientists and engineers* (Oxford University Press, 2015).

[38]A. Chaudhuri, A. Hadjadj, A. Chinnayya, and S. Palerm, "Numerical study of compressible mixing layers using high-order WENO schemes," J. Sci. Comput. **47**, 170–197 (2011).

[39]L. Davidson, "Transport equations in incompressible urans and les," in *Publication 2006/01, Chalmers University of Technology* (2006).

[40]M. S. Chong, A. E. Perry, and B. J. Cantwell, "A general classification of threedimensional flow fields," Phys. Fluids A **2**, 765–777 (1990).

[41]S. Pirozzoli and F. Grasso, "Direct numerical simulations of isotropic compressible turbulence: Influence of compressibility on dynamics and structures," Phys. Fluids **16**, 4386–4407 (2004).

[42]N. S. Vaghefi and C. K. Madnia, "Local flow topology and velocity gradient invariants in compressible turbulent mixing layer," J. Fluid Mech. **774**, 67–94 (2015).

[43]J. Wang, Y. Shi, L.-P. Wang, Z. Xiao, X. T. He, and S. Chen, "Effect of compressibility on the small-scale structures in isotropic turbulence," J. Fluid Mech. **713**, 588–631 (2012).

[44]S. Suman and S. S. Girimaji, "Velocity gradient invariants and local flow-field topology in compressible turbulence," J. Turbul. **11**, N2 (2010), https://doi.org/10.1080/14685241003604751.

[45]K. Kumari, S. Mahapatra, S. Ghosh, and J. Mathew, "Invariants of velocity gradient tensor in supersonic turbulent pipe, nozzle, and diffuser flows," Phys. Fluids **30**, 015104 (2018), https://doi.org/10.1063/1.5004468.

[46]J. Gaviglio, J. Dussauge, J. Debieve, and A. Favre, "Behavior of a turbulent flow, strongly out of equilibrium, at supersonic speeds," Phys. Fluids **20**, S179–S192 (1977), https://aip.scitation.org/doi/pdf/10.1063/1.861728.

[47]J. P. Dussauge, J. Gaviglio, and A. Favre, "Density changes and turbulence production in the expansion or compression of a turbulent flow at supersonic speed," in *Structure and Mechanisms of Turbulence II*, edited by H. Fiedler (Springer Berlin Heidelberg, Berlin,

Heidelberg, 1978) pp. 385–395.

[48]G.-H. Cottet, D. Jiroveanu, and B. Michaux, "Vorticity dynamics and turbulence models for large-eddy simulations," ESAIM-Math. Model. Num. **37**, 187–207 (2003).

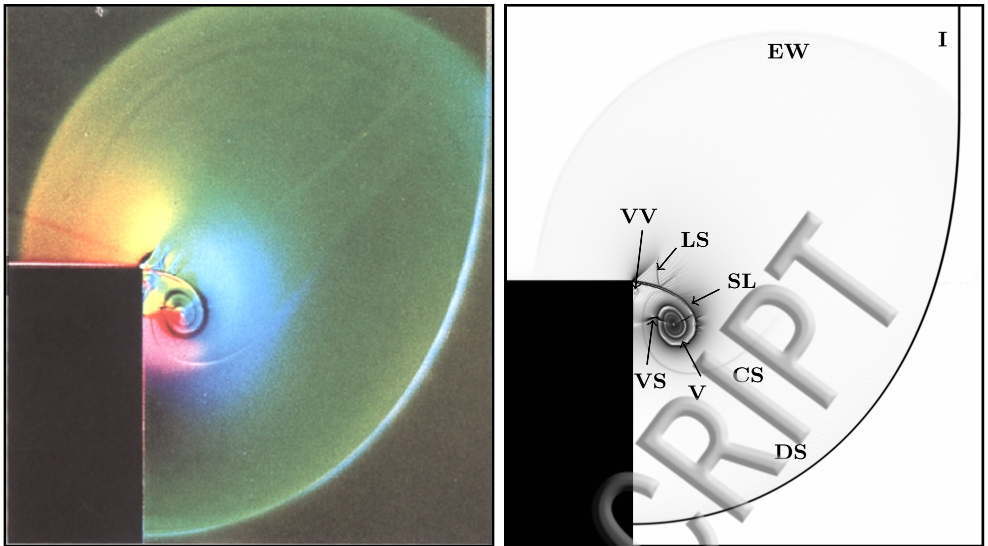

(a) Experiment, Ritzerfeld et al.[24] (b) Schlieren: present LES

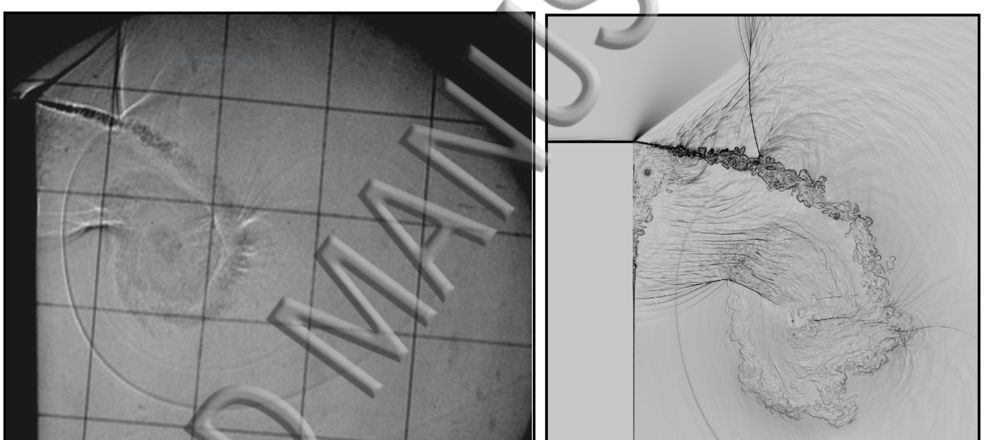

(c) Experiment, Skews et al.[25] (d) Schlieren: present LES

FIG. 2: Comparison of the flow features of the shock wave diffraction: top row: at early stage, and bottom row: at later stage. See table II for nomenclature. Figure (a) reproduced with permission from K. Takayama and O. Inoue, Shock wave diffraction over a 90 degree sharp corner – Posters presented at 18th ISSW, Shock waves 1, 301–312 (1991). Copyright 1991 Springer-Verlag. Figure (c) reproduced with permission from B. Skews, C. Law, A. Muritala, and S. Bode, Shear layer behavior resulting from shock wave diffraction, Exp. Fluids 52, 417–424 (2012). Copyright 2011 Springer-Verlag.

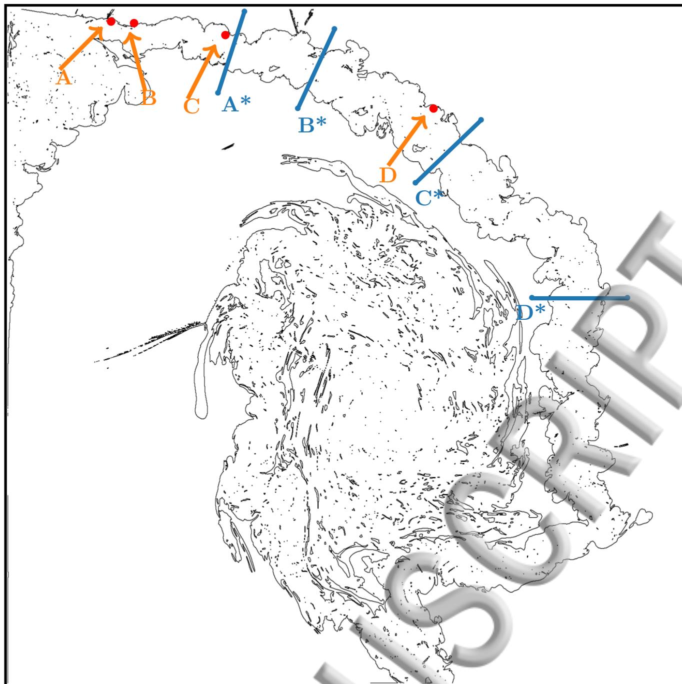

FIG. 3: Locations of probes/segments over a turbulent-nonturbulent interface (TNTI) contour for the computation of convective Mach number, two-point correlation, and normalized energy spectra.

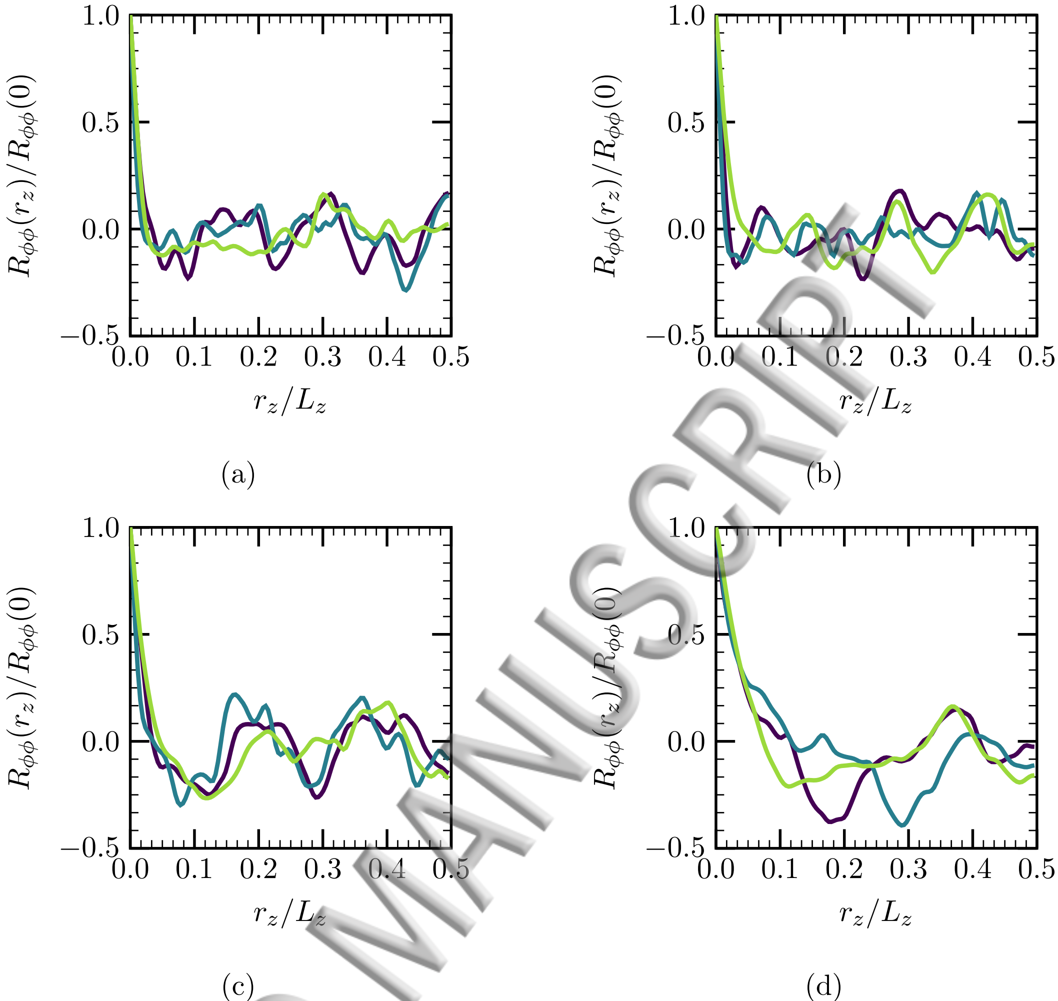

FIG. 4: Two-point correlation evaluation at $t = 757.75\mu s$: (a) – location A, (b) – location B, (c) – location C, (d) – location D. ▬ : u, ▬ : v, ▬ : w.

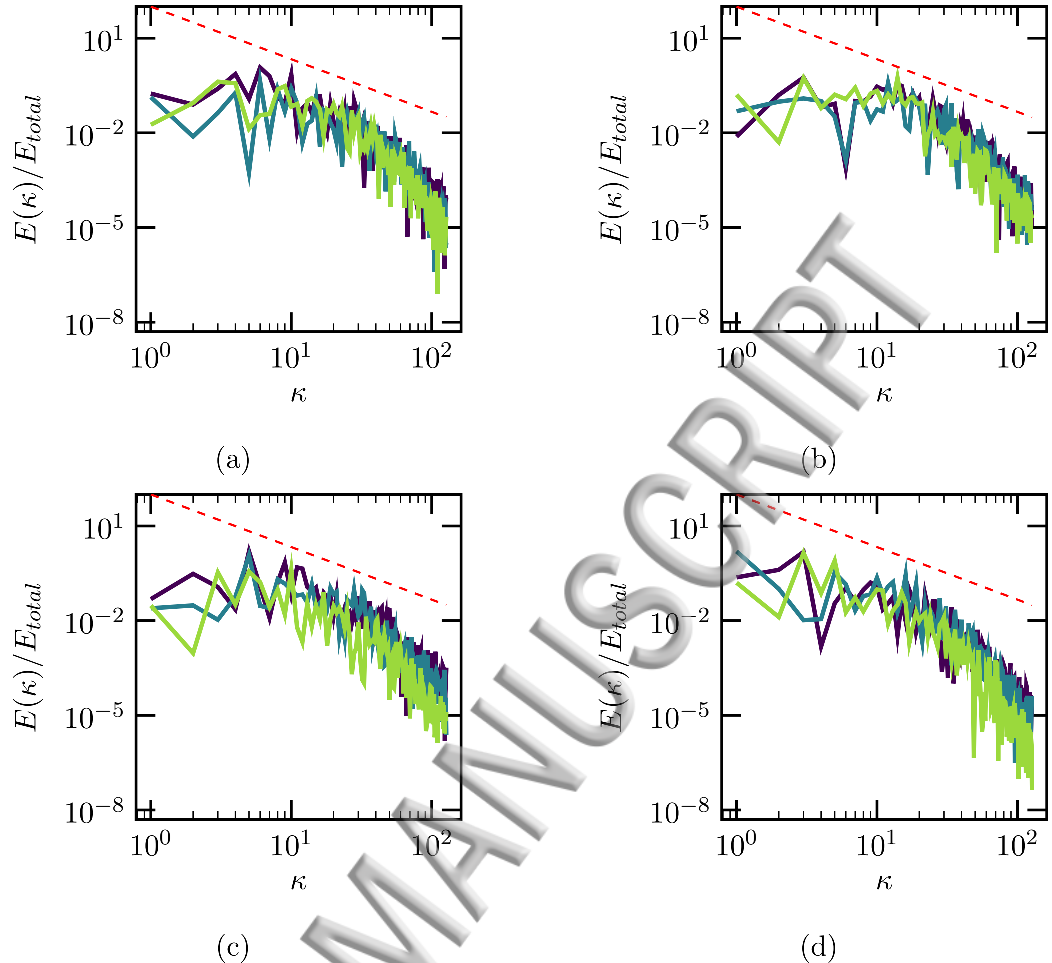

FIG. 5: Normalized energy spectra with wavenumber κ, at $t = 757.75\ \mu s$ in the homogeneous direction: (a) – location A, (b) – location B, (c) – location C, (d) – location D. — : u, — : v, — : w, - - - : $-5/3$ law.

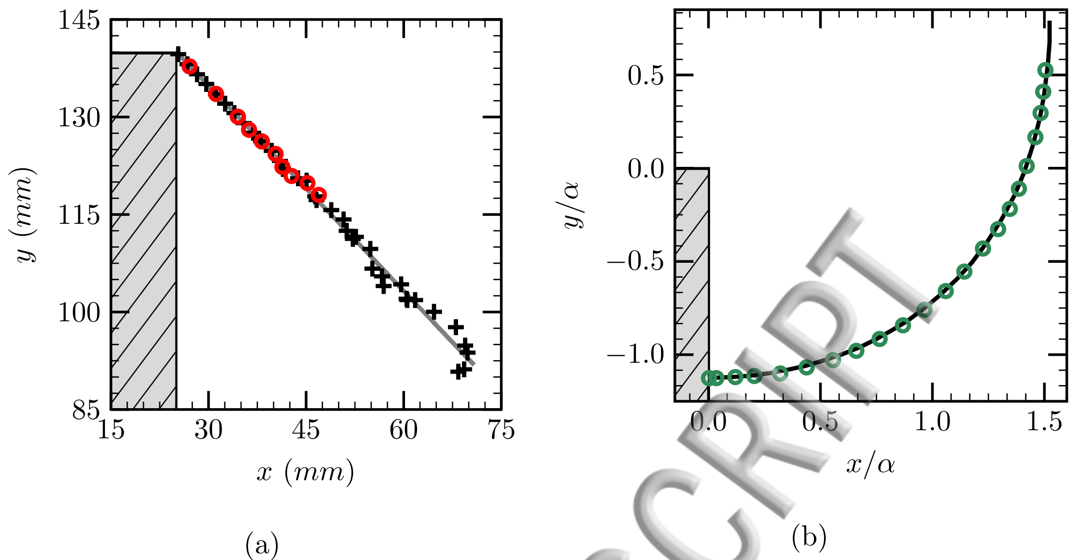

FIG. 6: (a) Location of the vortex centroid. + : centroid path (simulation), — : mean path, o : numerical data[6]. (b) Diffracted shock wave location (here, $\alpha = a_0 t$, a_0 is the speed of sound at the stagnant state). — : simulation data, o : experimental data[30].

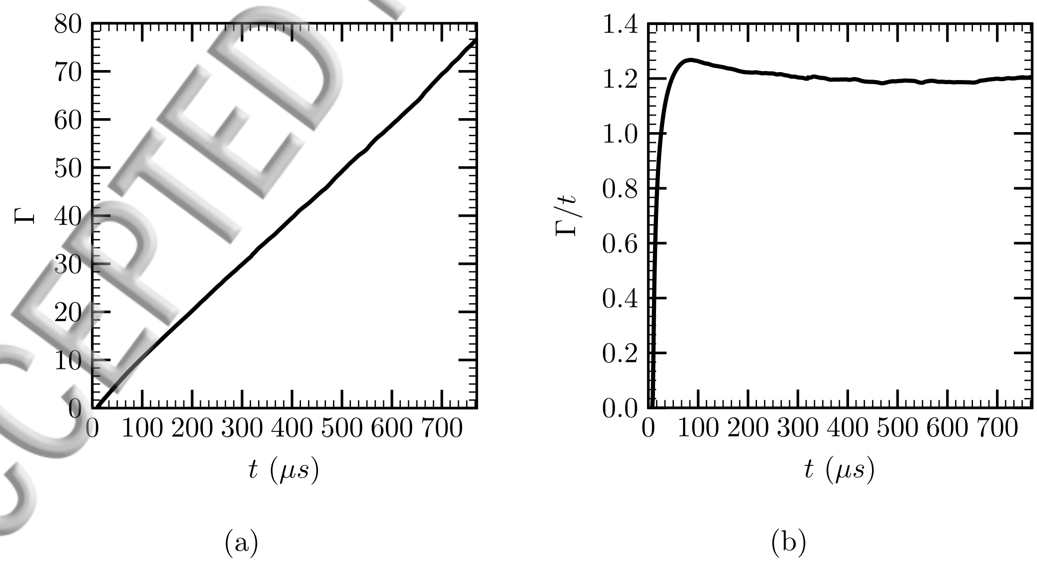

FIG. 7: Time evolution of (a) circulation (Γ). (b) circulation rate (Γ/t).

FIG. 8: Iso-surfaces of $\Lambda = 0.5$ at $t = 757.75$ μs colored with the enstrophy.

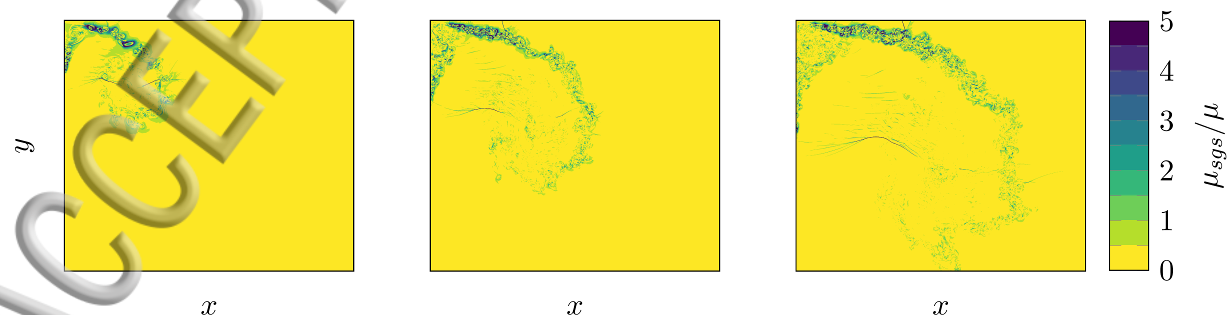

FIG. 9: μ_{sgs}/μ of a slice at $t = 339.75, 537.75$, and 757.75 μs column-wise, respectively.

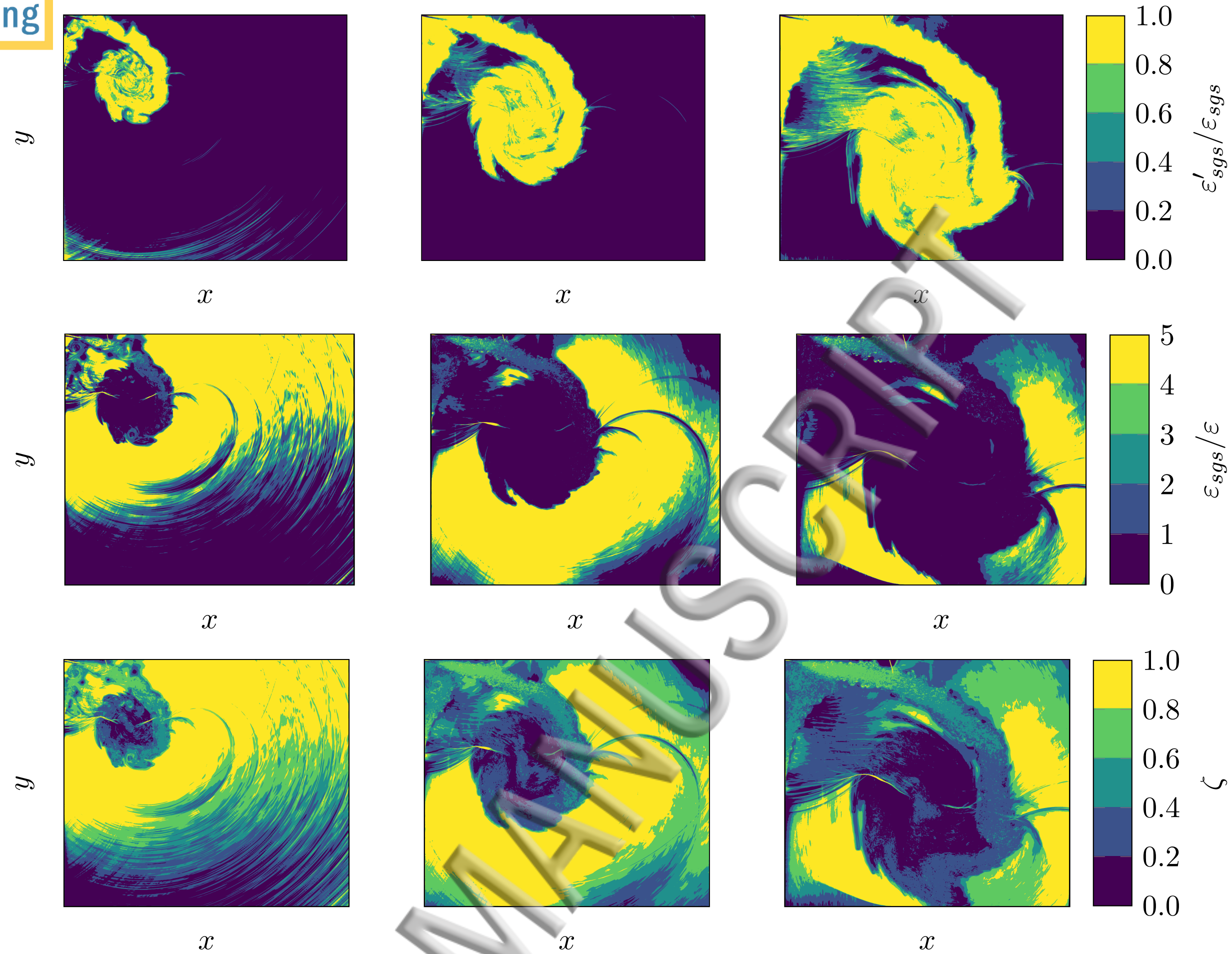

FIG. 10: Different subgrid-scale dissipation terms at $t = 339.75, 537.75$, and 757.75 μs column-wise, respectively.

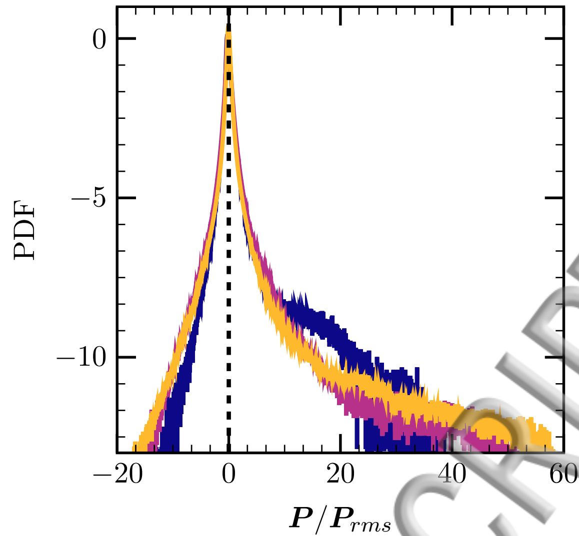

FIG. 11: PDF plot of the normalised first invariant of velocity gradient tensor in the entire turbulent region at $t = 251.75$(—), 449.75(—), and 757.75(—) μs.

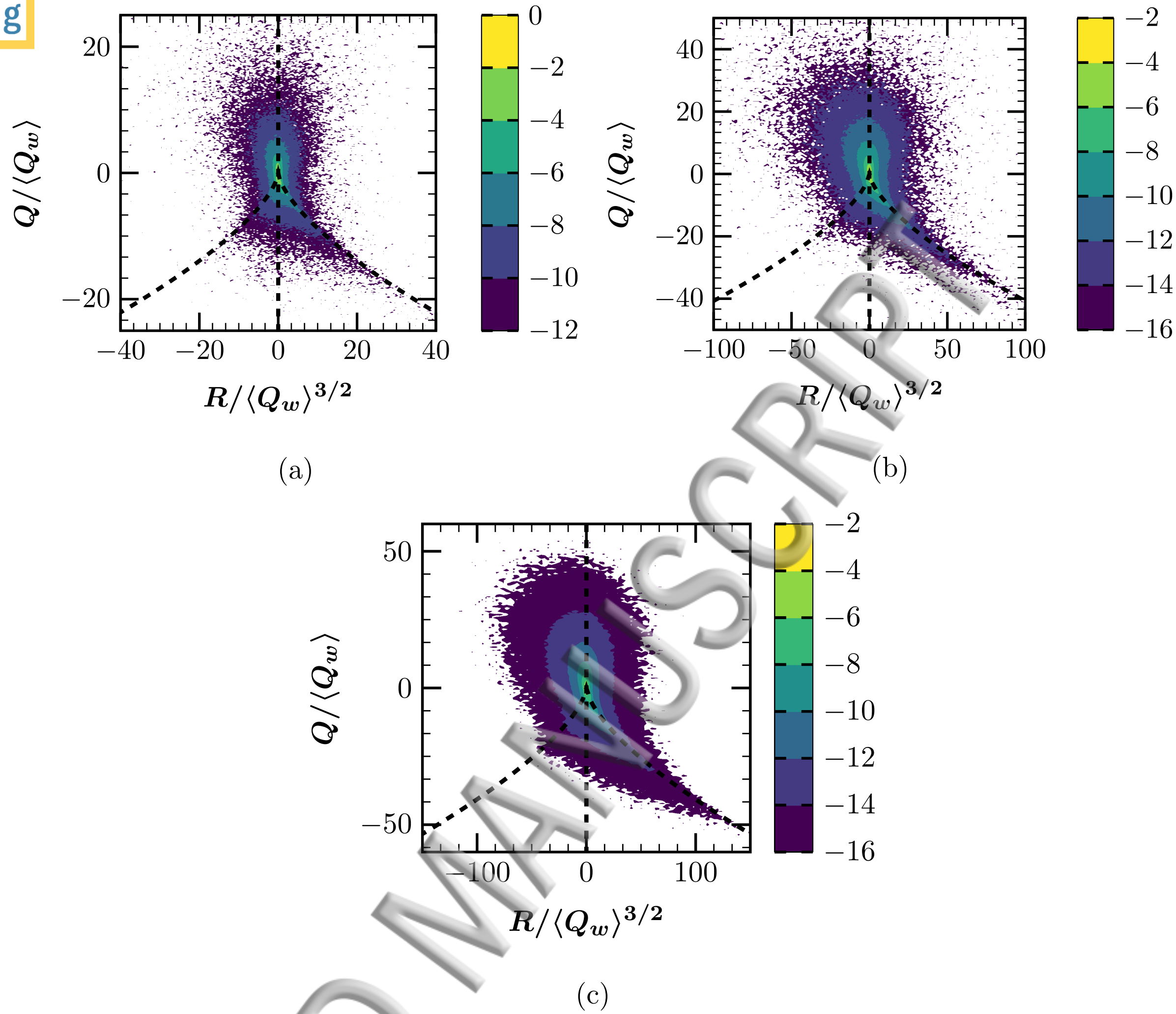

FIG. 12: JPDF plot of the normalised second and third invariants of velocity gradient tensor in the entire turbulent (TNTI) region at $t = 251.75, 449.75$, and $757.75\mu s$ for $\boldsymbol{P} = 0 \pm 0.05$.

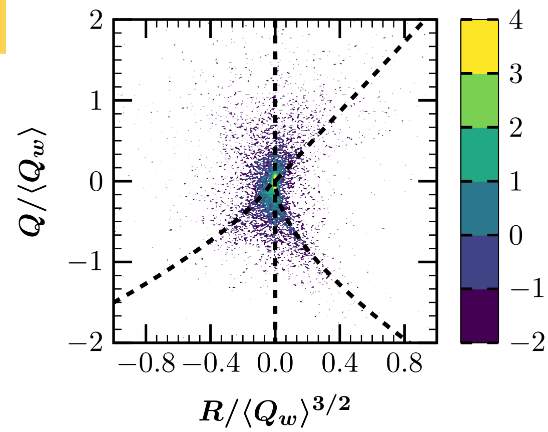

(a)

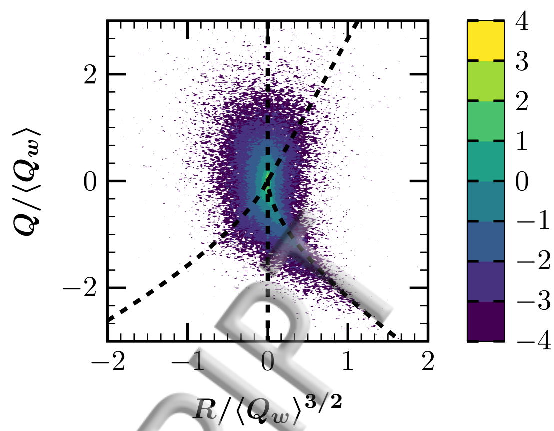

(b)

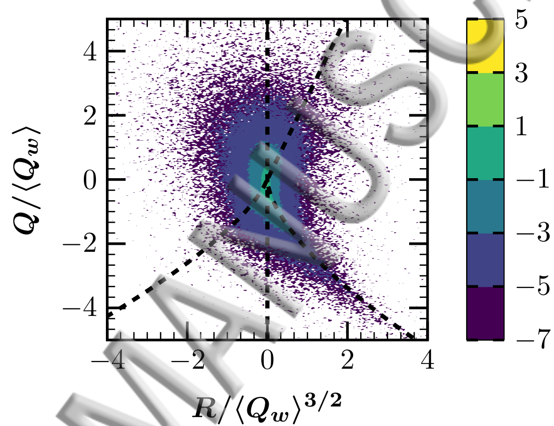

(c)

FIG. 13: JPDF plot of the normalised second and third invariants of velocity gradient tensor in the entire turbulent (TNTI) region at $t = 251.75, 449.75,$ and $757.75\mu s$ for $\boldsymbol{P} = 3 \pm 0.25$.

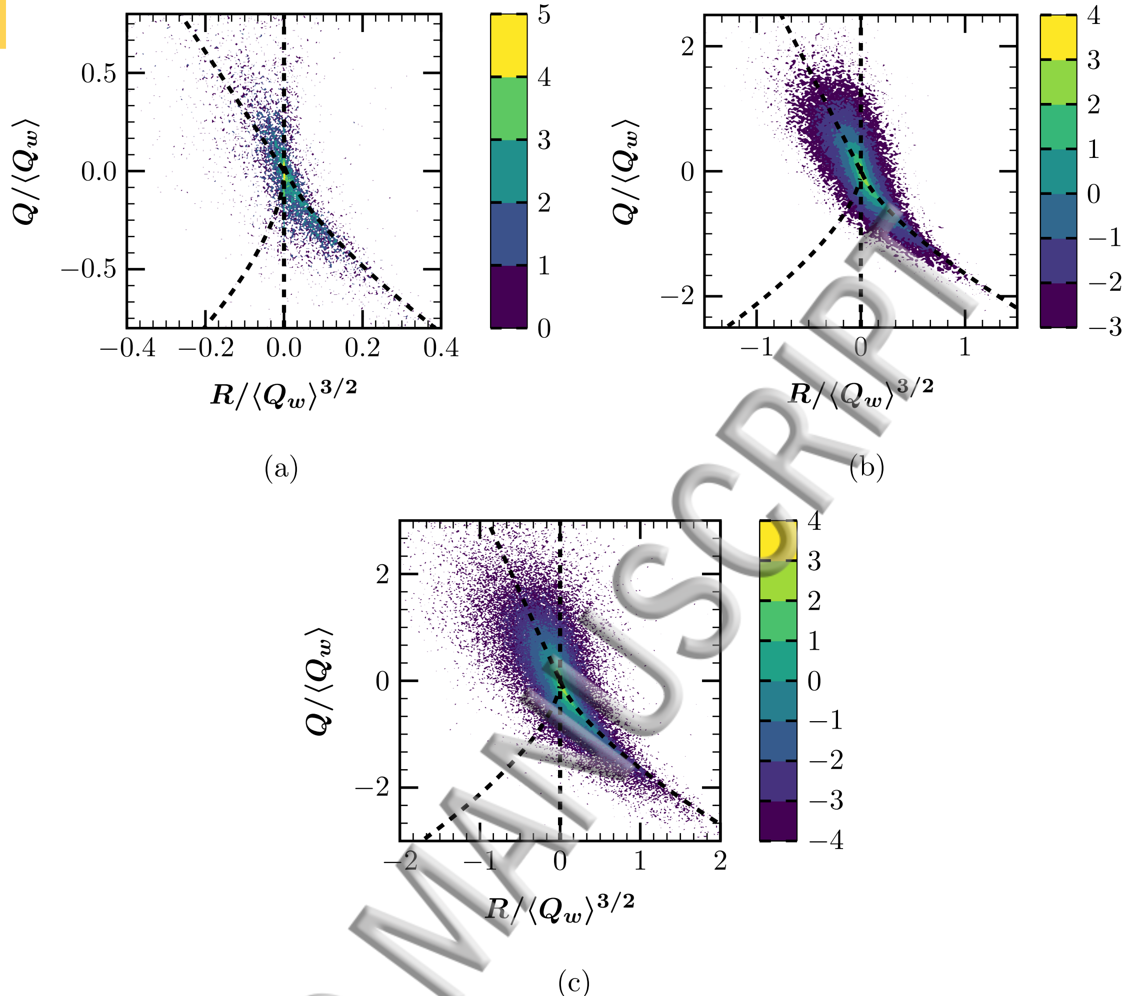

FIG. 14: JPDF plot of the normalised second and third invariants of velocity gradient tensor in the entire turbulent (TNTI) region at $t = 251.75, 449.75$, and $757.75\mu s$ for $\boldsymbol{P} = -3 \pm 0.05$.

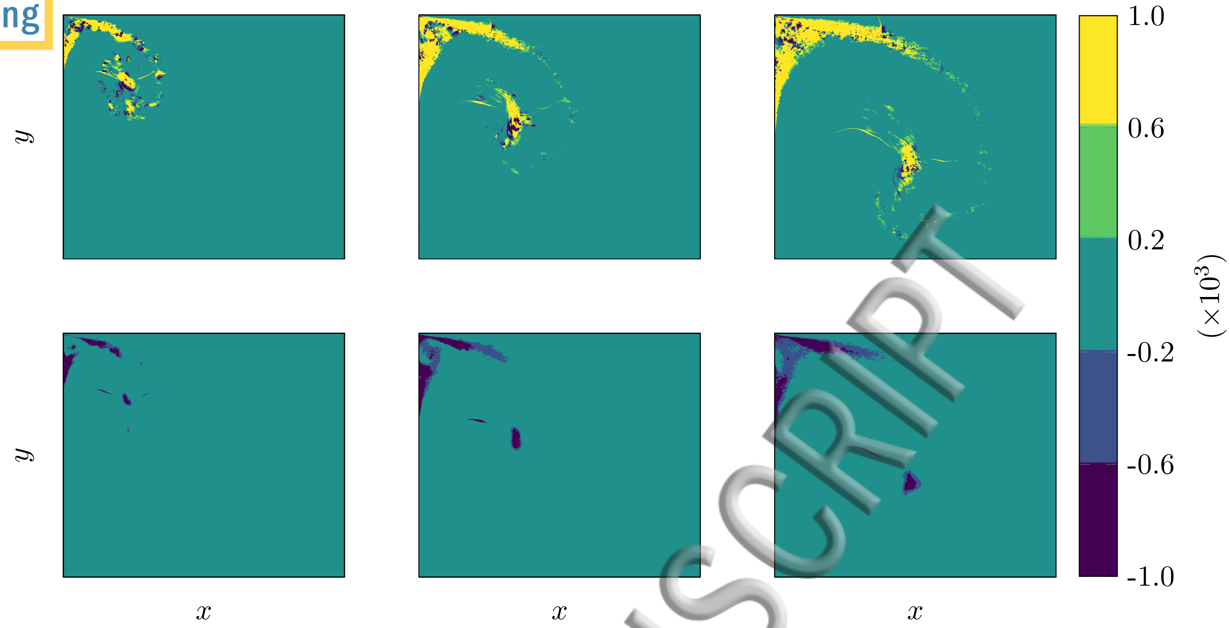

FIG. 15: TKE budget. Row-wise (top-to-bottom): production and dissipation terms. Column-wise (left-to-right): $t = 339.75, 537.75$, and 757.75 μs.

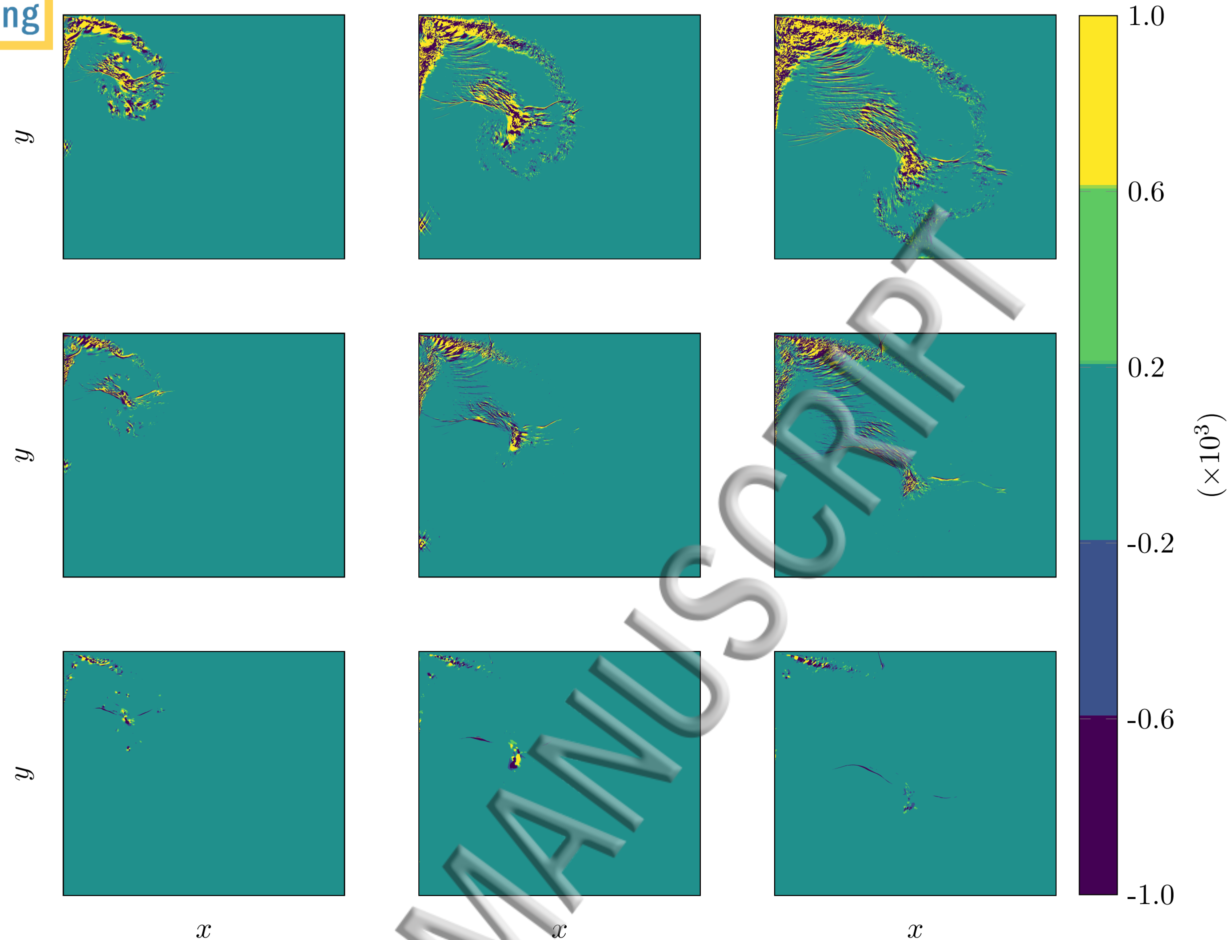

FIG. 16: TKE budget. Row-wise (top-to-bottom): diffusion, pressure-dilatation, and pressure-work terms. Column-wise (left-to-right): $t = 339.75, 537.75$, and 757.75 μs.

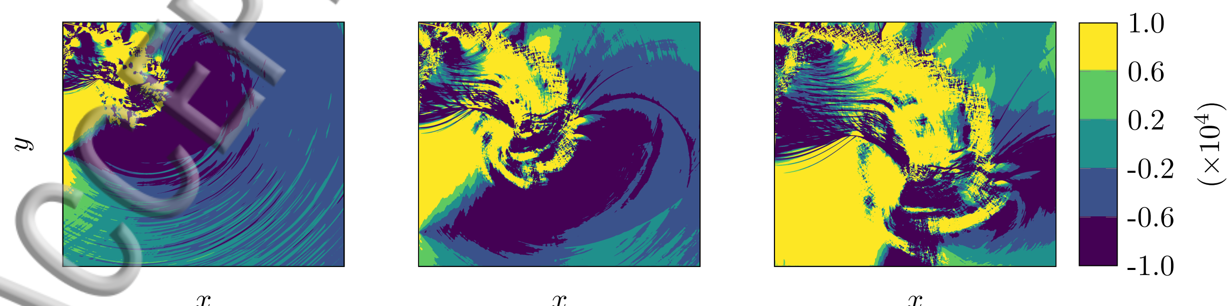

FIG. 17: TKE budget - advection term. Column-wise (left-to-right): $t = 339.75, 537.75$, and 757.75 μs.

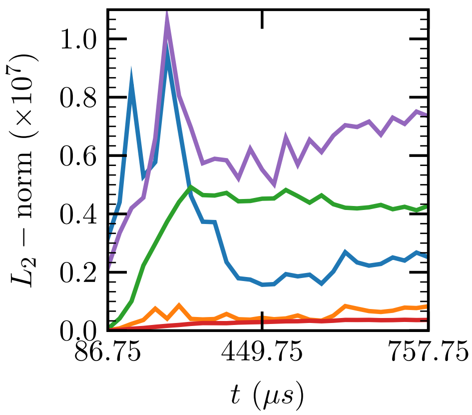

(a)

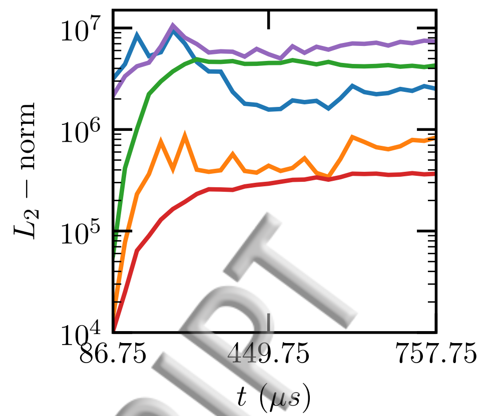

(b)

FIG. 18: Norm of TKE budget terms as a function of time (a) linear-scale, and (b) logarithmic-scale. — : pressure-dilatation, — : pressure-work, — : production, — : dissipation, — : diffusion.

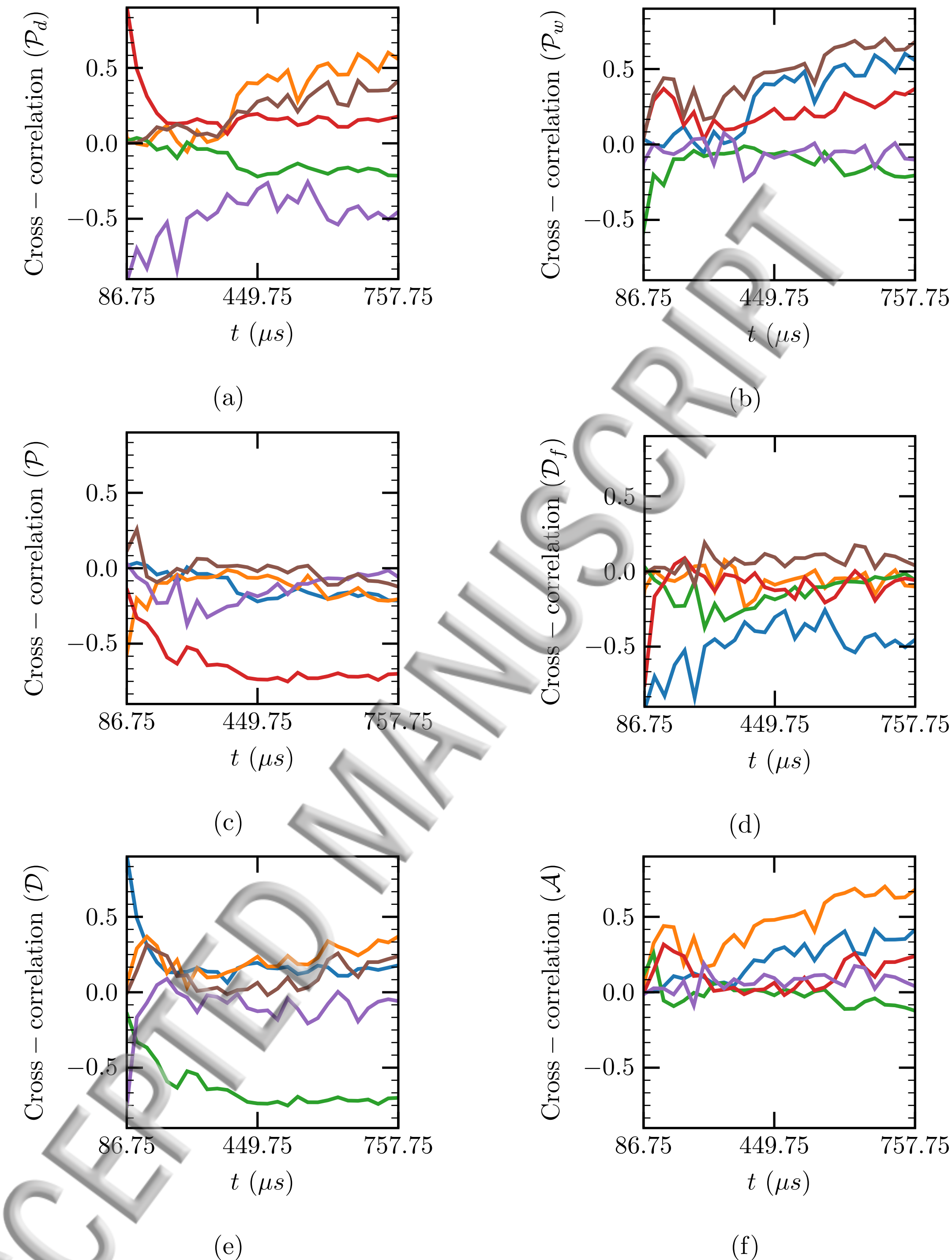

FIG. 19: Spatial cross-correlation of (a) pressure-dilatation ($\mathcal{P}_d$), (b) pressure-work ($\mathcal{P}_w$), (c) production ($\mathcal{P}$), (d) diffusion ($\mathcal{D}_f$), (e) dissipation ($\mathcal{D}$), and (f) advection ($\mathcal{A}$) terms of TKE budget with each other in time. — : pressure-dilatation, — : pressure-work, — : production, — : dissipation, — : diffusion, — : advection.

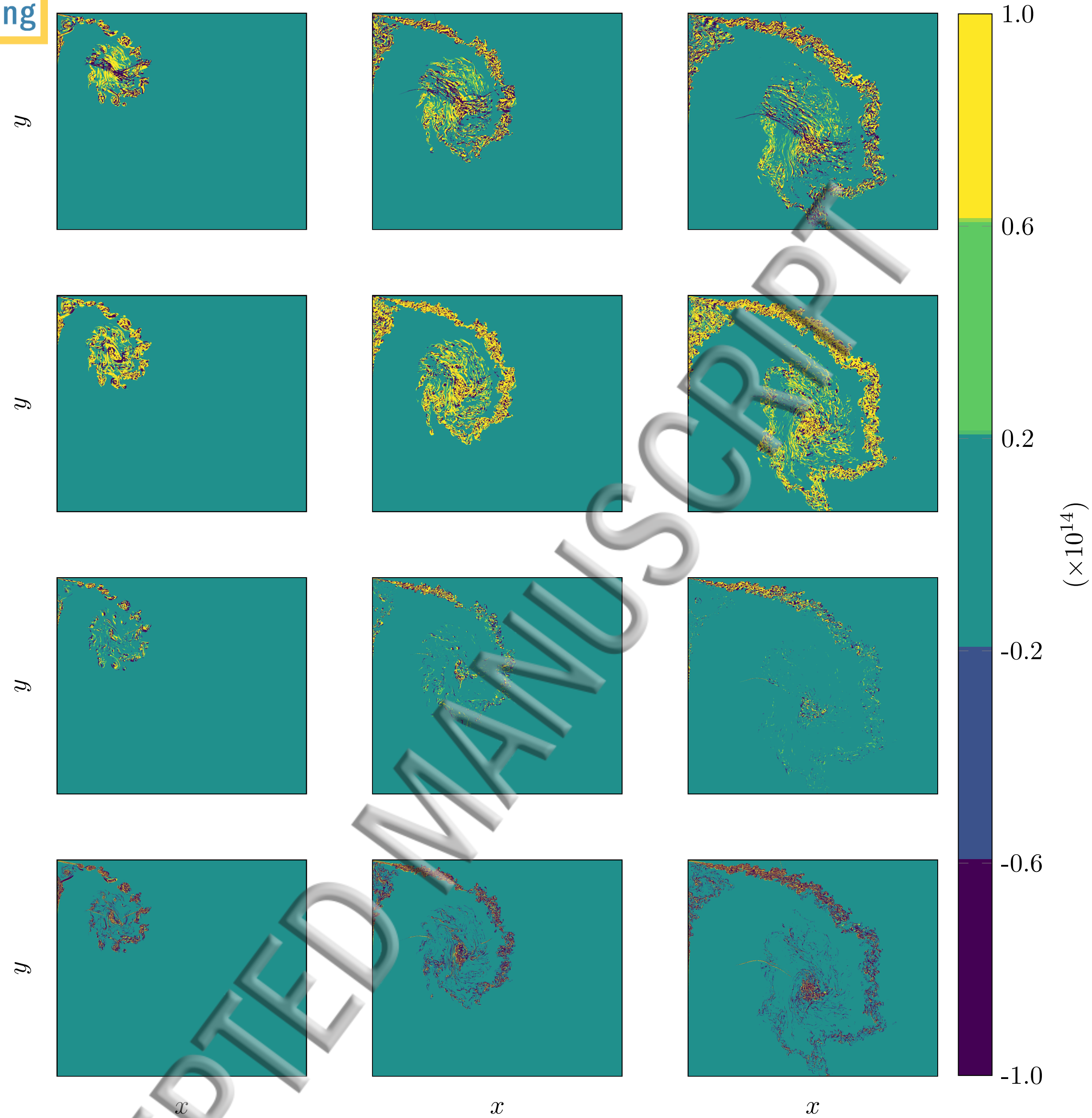

FIG. 20: VTE budget. Row-wise (top-to-bottom): VSC, VSG, baroclinic, and DFV terms. Column-wise (left-to-right): $t = 339.75, 537.75$, and 757.75 μs.

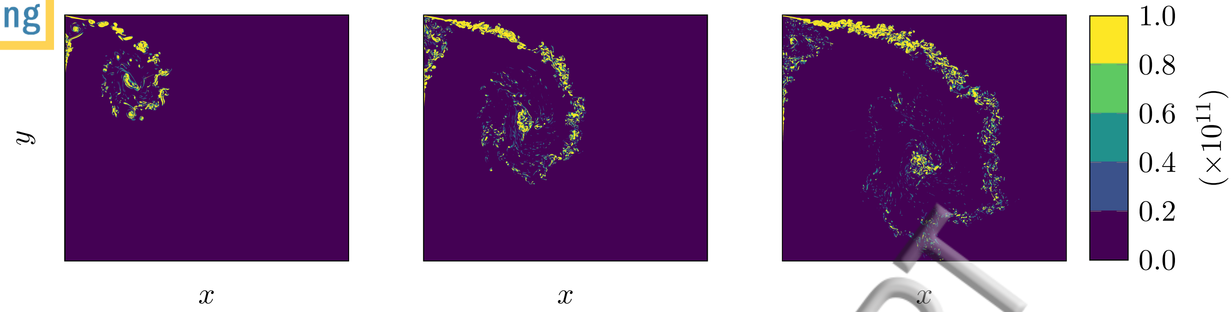

FIG. 21: Enstrophy contour. Column-wise (left-to-right): $t = 339.75, 537.75$, and $757.75\ \mu s$.

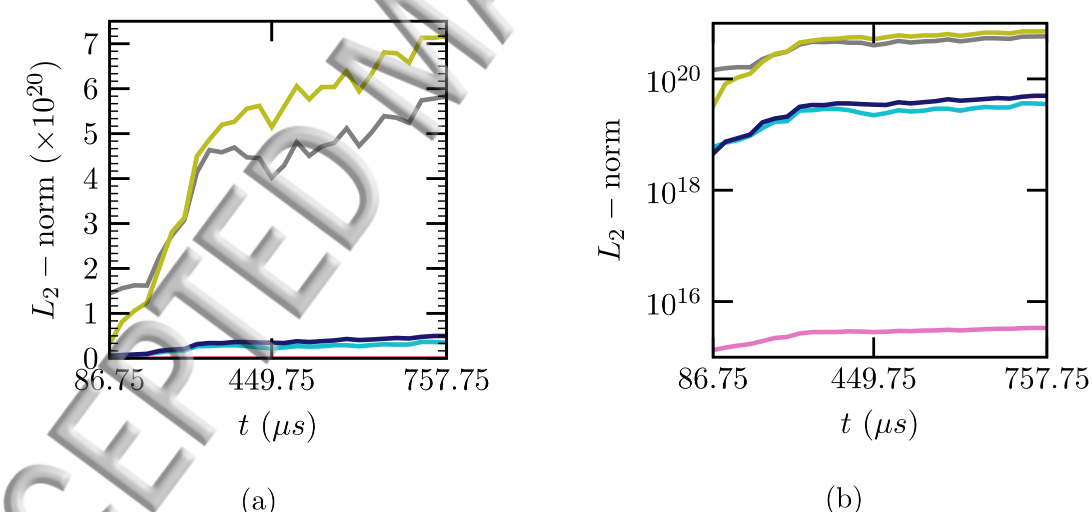

FIG. 22: Norm of VTE budget terms as a function of time (a) linear-scale, and (b) logarithmic-scale. — : enstrophy, — : VSC, — : VSG, — : baroclinic, — : DFV.

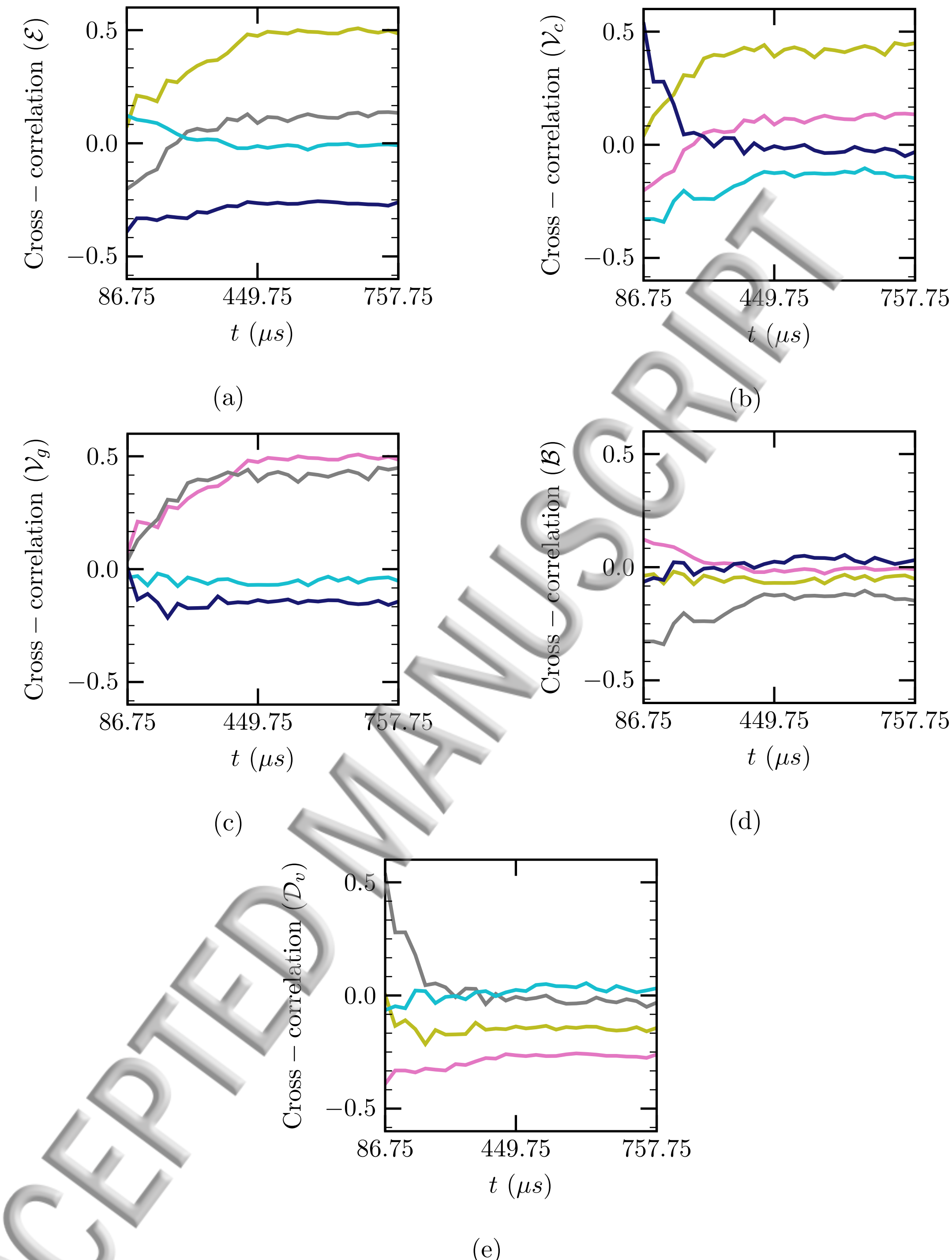

FIG. 23: Spatial cross-correlation of (a) enstrophy ($\mathcal{E}$), (b) VSC ($\mathcal{V}_c$), (c) VSG ($\mathcal{V}_g$), (d) baroclinic ($\mathcal{B}$), and (e) DFV ($\mathcal{D}_v$) terms of VTE budget with each other in time. — : enstrophy, — : VSC, — : VSG, — : baroclinic, — : DFV.